Anomalous Small-Angle X-ray Scattering Characterization of Bulk Block Copolymer/Nanoparticle Composites

Byeongdu Lee,*,† Chieh-Tsung Lo,† Soenke Seifert,† Nancy L. Dietz Rago,‡ Randall E. Winans,†,§ and Pappannan Thiyagarajan⊥,*

X-ray Science Division, Chemical Engineering Division, Chemistry Division, and Intense Pulsed Neutron Source, Argonne National Laboratory, 9700 S. Cass Ave., Argonne, Illinois 60439

Received December 19, 2006; Revised Manuscript Received February 16, 2007

ABSTRACT: We demonstrate the versatility of anomalous small-angle X-ray scattering (ASAXS) to investigate the morphology of bulk multicomponent composites comprising poly(stryrene-*b*-2-vinylpyridine) (PS−PVP) and Au nanoparticles. Contrast variation near the L_3 absorption edge of Au enables the separation of the partial scattering functions of the polymer and nanoparticle phases. Theoretical and experimental methodologies developed for our ASAXS analysis of the composites will be useful for the investigation of other such multicomponent systems with heavy elements. This study shows that at 8.8% Au loading the Au nanoparticles remain well dispersed in the lamellar polymer matrix, while at 27.0% Au loading the polymer morphology transforms to a hexagonal packed cylinder phase due to the change in the curvature caused by the higher concentration of the dispersed nanoparticles in the PS domain. In the case of 27.0% Au nanocomposite we also observe strong concentration fluctuations of nanoparticles in the polymer phase, with a hierarchical structure containing mass fractal aggregates and particle−particle correlation as evidenced by the $Q^{-2.4}$ power law scattering in the low Q and a liquid-like peak at the high Q regions of the scattering signal from the nanoparticles.

Introduction

Nanocomposites offer as future advanced materials exploiting the unique electronic,[1,2] magnetic,[3] and mechanical properties[4] of the nanoparticles, and their synthesis requires the ability to control the state of dispersion and ordering of nanoparticles in appropriate matrices. Recently, block copolymers have been shown to serve as versatile platforms for dispersing nanoparticles in polymer matrices. This technique, based on the self-assembly of nanoparticles in one microdomain of the block copolymer followed by its microphase separation, enables the preparation of nanocomposites with particles organized in a variety of polymer morphologies. Although several theoretical[5−8] and experimental studies have been recently reported,[9−15] the morphologies of the polymer phase and the nature of dispersion of nanoparticles in the composites prepared at different conditions have not been thoroughly studied using neutron and X-ray scattering techniques that can provide more relevant statistically averaged information on the hierarchical nanostructural features in the composites.

The small-angle scattering techniques using X-rays (SAXS) and neutrons (SANS) are powerful tools to probe the nanoscale structural features in complex materials. Although the basic principles of scattering are the same, the contrasts are quite different for these probes. The differences between the scattering length densities in SANS and the electron densities in SAXS of particles and the surrounding matrix determine the scattering contrasts. The scattering contrast can be varied in SANS by manipulating the deuteration levels of either the solvent/matrix or solute or both. In multicomponent systems, contrast variation SANS with deuterium labeling enables the determination of the shapes and densities of the individual components by making a certain component visible or invisible to neutron scattering. A similar contrast variation can be done with SAXS by manipulating the electron density of the solvents using glycerol or sucrose, as done in the study of aqueous dispersion of ionic PS/PMMA latex particles.[16] However, only limited systems are amenable to this SAXS method.

Another contrast variation method that is unique to SAXS exploits the variation in the atomic scattering factor of elements near their X-ray absorption edges, and this is useful for the characterization of systems with high atomic number elements. In the vicinity of a characteristic X-ray absorption edge of an atom phase shift occurs between the absorbed and emitted rays. The magnitude of the phase shift depends on the power of its absorption that varies as a function of X-ray energy, known as the anomalous dispersion. In X-ray crystallography, multiwavelength anomalous diffraction (MAD),[17,18] wherein diffraction intensities are measured at different energies in the vicinity of an absorption edge of an element, has been widely used. The variation of intensities of reflections associated with the anomalous scatterer as a function of X-ray energy enables solving the phase problem.

The anomalous dispersion when applied to the SAXS region, anomalous small-angle X-ray scattering (ASAXS),[19] allows contrast variation that is useful for the characterization of nanostructured materials. On the basis of the extensive use of MAD technique in protein crystallography, it is reasonable to expect that the ASAXS was also widely used. However, its applications in materials research have been fairly limited due to the following reasons: (1) Unlike the MAD technique in protein crystallography with Se-labeled amino acid residues, the ASAXS can be applied only to a limited systems with high z (atomic number) elements intrinsic to the systems such as metallic alloys and composites wherein labeling is usually not an option. (2) Nanocomposites are complex; the measured data are convoluted by the form factors of multiple phases, and it is

* To whom all correspondence should be addressed. E-mail: blee@aps.anl.gov; thiyaga@anl.gov.
† X-ray Science Division.
‡ Chemical Engineering Division.
§ Chemistry Division.
⊥ Intense Pulsed Neutron Source.

10.1021/ma062916h CCC: $37.00
Published on Web 05/19/2007

more difficult to deconvolute the form factors than the structure factors in the diffraction regime as in the MAD technique. (3) The structures in the nanocomposites are less ordered or disordered, and since the measured wave vector space in SAXS is quite small, the data are useful more as a tool to vary the contrast to infer the presence of a given element rather than for detailed structural analysis. (4) Limited facilities that can provide high-energy resolution and precision to accurately measure both the absorption and scattering data as well as adequate data collection, data reduction, and analysis tools for the ASAXS experiments.

Recently, Dingenouts et al.[20] reported an ASAXS study of aqueous ionic solution of spherical polyelectrolyte brush composed of a solid polystyrene (PS) core and a shell consisting of densely grafted linear poly(acrylic acid) chains and rubidium counterions. They presented experimental and theoretical methodologies for a quantitative analysis of the structure factor associated with the core and shell as a function of X-ray energy that led to the determination of the electron density distribution along the radial direction from the particle core. Characterization of hybrid materials such as bulk copolymer/inorganic nanocomposites is far more challenging due to the fact that they have several scattering centers with different length scales and disorder. Depending on the structural features in these materials, different formalisms will be necessary to delineate the partial scattering functions of different species from the ASAXS data as described below.

Here we report the application of ASAXS to investigate the morphology of the polymer phases and the nature of dispersion of PSSH (thiol-terminated PS) tethered Au nanoparticles in bulk poly(styrene-*b*-2-vinylpyridine) (PS−PVP) diblock copolymer composites. We present a method to separate the partial scattering signals from the Au nanoparticles and the polymer phases from the measured ASAXS data of the nanocomposites. To demonstrate the efficacy of our ASAXS methodology, we use two nanocomposites with different Au loading as examples that represent two distinctly different organizations of particles in block copolymer matrices.

Theory

In general, the contrast that contributes to the SAXS signals is the square of the electron density difference between the particles and the matrix. The electron density of the particles or matrix at an X-ray energy E can be calculated using

$$\rho_e = \sum_i^N n_i f_i(Q=0,E) \tag{1}$$

where the scattering vector $Q = 4\pi \sin\theta/\lambda$; 2θ is the scattering angle and λ the wavelength of X-rays, and n_i and f_i are the number density and the scattering factor of i^{th} atom among N types of atoms in a domain. In the case of polymers, $n_i = N_i \rho N_A / M$, where N_i and M are the number of i^{th} atoms in a monomeric unit and total molecular weight of the unit, respectively, ρ is the bulk density, and N_A is the Avogadro number. In PS−PVP nanocomposites with Au particles dispersed solely in the PS domain SAXS signals arise from two different scattering sources: the electron density difference between Au and the surrounding PS, $\rho_g(E) \equiv \rho_{e,Au} - \rho_{e,PS}$, and that between PS and PVP in the block copolymer, $\rho_b \equiv \rho_{e,PVP} - \bar{\rho}_{e,PS/Au} = \rho_{b,0} - \upsilon_{Au}\rho_g$, where $\rho_{b,0} \equiv \rho_{e,PVP} - \rho_{e,PS}$ and $\bar{\rho}_{e,PS/Au}$ is the average electron density of the PS domain containing Au whose volume fraction is υ_{Au} in the domain. The electron densities of Au and PS respectively are $\rho_{e,Au}(E) = n_{Au} f_{Au}(E)$ and $\rho_{e,PS}(E) = n_C f_C(E) + n_H f_H(E)$, where C and H correspond to carbon and hydrogen atoms. The electron densities of PS and PVP are 0.340 and 0.366 Å^{-3}, respectively, and they are energy-independent at X-ray energies near the L edges of Au. On the basis of a face-centered-cubic phase of Au with a unit cell dimension of 4.078 Å and $n_{Au} \sim 0.059$ Å^{-3}, its electron density is ~4.66 Å^{-3} at energies far away from its absorption edge where the anomalous dispersion is negligible.

In the vicinity of an absorption edge of an element, the atomic scattering factor strongly depends on the X-ray energy (E)

$$\begin{aligned} f_{Au}(E) &= f_{0,Au} + f'_{Au}(E) + if''_{Au}(E) \\ &= f_{1,Au}(E) + if''_{Au}(E) \end{aligned} \tag{2}$$

where f_0 is the nonresonant term and f' and f'' are the energy-dependent real and imaginary parts of anomalous dispersion. In the case of ASAXS experiments of the PS−PVP/Au composites the scattering contrast can be varied by measuring the SAXS data using different incident X-ray energies in the vicinity of the L_3 absorption edge of Au. To obtain the partial scattering functions from the measured ASAXS data of the composites, we develop formalisms for two scenarios—case I: PSSH tethered Au nanoparticles are dispersed only in the PS domain of the block copolymer (see Figure 1a); case II: particles do not disperse in the polymer matrix but form macrophase-separated domains (see Figure 1d).[19,21]

Case I. For the bulk composites with well-dispersed Au nanoparticles in the PS domain of PS−PVP (see Figure 1a), the conventional SAXS intensity can be expressed as

$$\begin{aligned} I(Q) &= S_b(Q)|\rho_b F_b(Q) + \rho_g F_g(Q)|^2 \\ &= S_b(Q)(\rho_b{}^2 F_b{}^2 + 2\rho_b \rho_g F_b F_g + \rho_g{}^2 F_g{}^2) \end{aligned} \tag{3}$$

where $S_b(Q)$ is the structure factor of the block copolymer, $F_b(Q)$ is the scattering amplitude of the copolymer, and $F_g(Q) = F_{1,g}(Q)\sum_i^N e^{-iQd_i}$ is the scattering amplitude of the dispersed Au nanoparticles, where N is the number of Au particles in the PS domain, d_i is the relative distance of ith particle from the center of mass of the PS domain, and $F_{1,g}(Q)$ is the form factor of a single Au nanoparticle.

For the ASAXS experiments near the absorption edge of Au, eq 3 can be expressed as a function of nonresonant and resonant terms:

$$\begin{aligned} I(Q,E) &= S_b(Q)(F_{NR} + n_{Au} f'_{Au}(E)[F_g(Q) - \upsilon_{Au} F_b(Q)])^2 \\ &= S_b(Q)(F_{NR}{}^2 + 2n_{Au} F_{NR}[F_g(Q) - \upsilon_{Au} F_b(Q)] f'_{Au}(E) + \\ &\qquad n_{Au}{}^2 [F_g(Q) - \upsilon_{Au} F_b(Q)]^2 f'_{Au}{}^2(E)) \end{aligned} \tag{4}$$

where $F_{NR} = \rho_{b,0} F_b + (n_{Au} f_{0,Au} - \rho_{e,PS})(F_g - \upsilon_{Au} F_b)$ and $f_{0,Au}$ is the nonresonant term of the scattering factor of Au. It can be seen that eq 4 is similar to eq 12 in Dingenouts et al.,[20] except for the imaginary term of the anomalous dispersion that has been neglected due to its extremely small contribution to the scattering signal. For a well-dispersed system the structure factor of the block copolymer ($S_b(Q)$) convolutes (see eq 4) with both the scattering intensity of the Au particles and the cross-terms involving the scattering amplitudes of the Au particle (F_g) and the polymer matrix (F_b). Since the cross-term has information on the relative position of particles in the matrix, its extraction is the key to delineate information on the nature of dispersion of the particles.

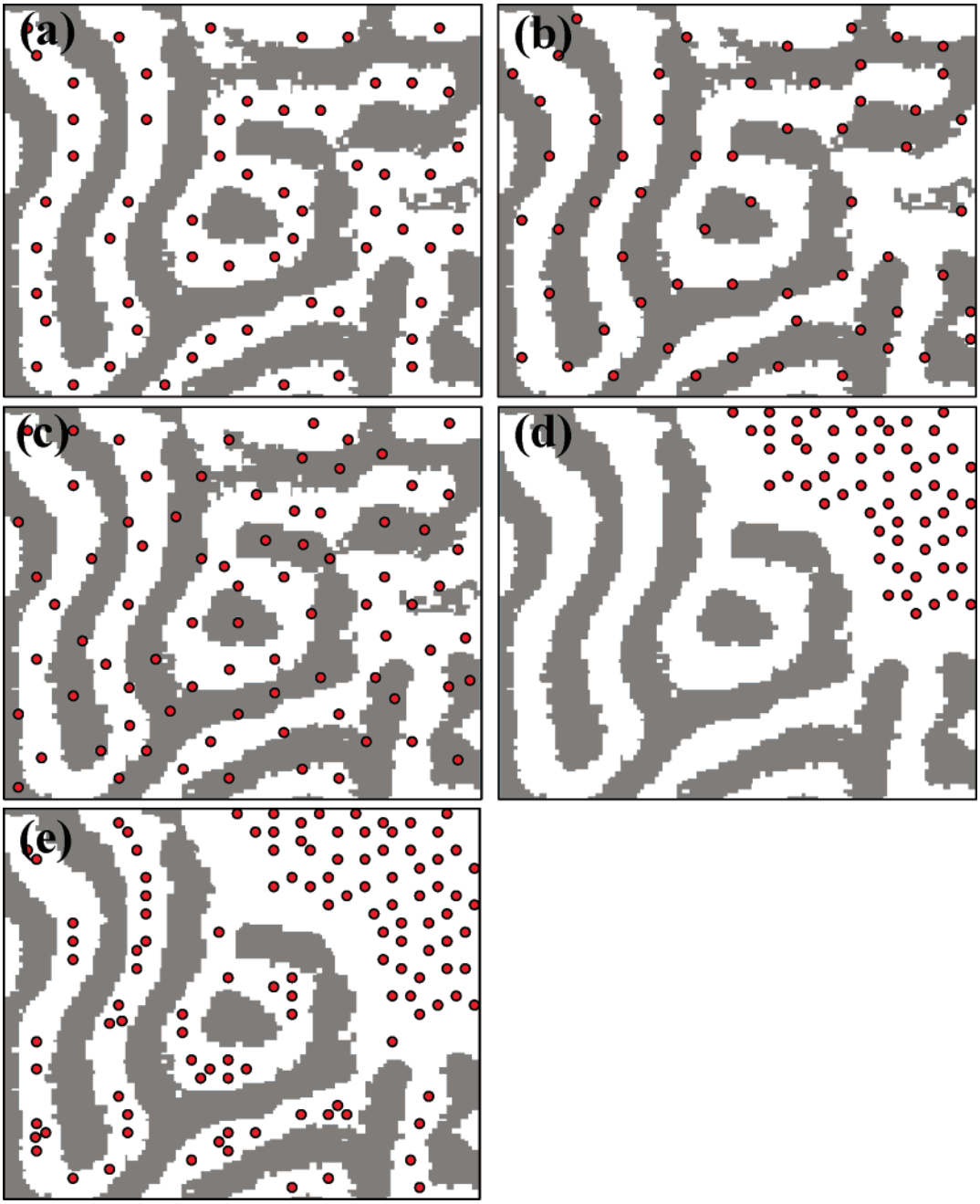

Figure 1. Schematic of the structural models of block copolymer/nanoparticle composites. Nanoparticle locations and the structure of the block copolymer are correlated: (a) particles are dispersed homogeneously in one domain of the block copolymer; (b) particles are located at the interface between the two phases of block copolymer. Nanoparticle locations and the structure of the block copolymer are uncorrelated: (c) particles randomly distributed in the matrix; (d) particles macrophase separated from the block copolymer. (e) Nanoparticles are well dispersed in one domain of the block copolymer, and the excess form macrophase-separated domains.

Case II. In composites consisting of a polymer phase and a macrophase-separated domain of nanoparticles (see Figure 1d), the SAXS signal is the sum of the contributions from the polymer phase and the PSSH tethered Au particles:

$$I(Q) = \rho_{b,0}{}^2 F_0{}^2(Q) + \rho_g{}^2 F_g{}^2(Q) \quad (5)$$

Equation 5 as a function of nonresonant and resonant terms relevant to the ASAXS experiments becomes

$$I(Q,E) = I_{NR}(Q) + 2n_{Au}(n_{Au}f_{0,Au} - \rho_{e,PS})F_g{}^2(Q)f'_{Au}(E) + n_{Au}{}^2 F_g{}^2(Q)f'_{Au}{}^2(E) \quad (6)$$

where $I_{NR} = \rho_{b,0}{}^2 S_b(Q)F_b{}^2(Q) + (n_{Au}f_{0,Au} - \rho_{e,PS})^2 F_g{}^2$. It can be seen that eqs 4 and 6 are second-order polynomials of f', but with different coefficients. In eq 6 $S_b(Q)$ does not convolute with the scattering signal of Au particles. Hence, the scattering signals for the polymer and nanoparticle phases can be separated by a simple subtraction of the SAXS data measured at two different X-ray energies, for example, one near and another ~200 eV below the edge where the resonance effect is negligible.

Intermediate situations such as particles dispersed at the interfaces of the microphase-separated PS and PVP domains (Figure 1b), random distribution of the nanoparticles in the polymer matrix (Figure 1c), and particles existing as dispersed

in the polymer phase as well as macrophase separated (Figure 1e) can be dealt with using the formalisms for cases I and II. The major difference between cases I and II is the existence of correlation between the structure of block copolymer and positions of nanoparticles. Models in Figure 1a,b belong to case I, those in Figure 1c,d to case II, and that in Figure 1e to the combination of both case I and case II. Below we show that ASAXS can readily elucidate the structural characteristics of the particle and polymer phases with the complex system in Figure 1e.

Analysis

Equations 4 and 6 are quadratic forms of f' whose values can be measured experimentally (see next section) or taken from McMaster tables,[22,23] and the coefficients of f' can be derived by fitting the measured scattering intensity values at different X-ray energies at a given Q. For the fitting method with a quadratic equation to work well, the measured scattering intensities as a function of f' in a given energy range should exhibit a nonlinear behavior. It should be noted that f' varies strongly only at energies very close to the edge and f'' hardly varies below the edge (see Figure 2 in Dingenouts et al.[20]). If the f' values are taken from the McMaster tables, they have to be smeared for the finite energy resolution of the monochromator, and the effective f' values as a function of incident X-ray energy should be used for fitting the ASAXS data. However, the extracted coefficients should be associated with either eq 4 for the correlated structures (case I) or eq 6 for the uncorrelated structures (case II) on the basis of the proposed models for the system. In addition, if the intensities at a given Q as a function of effective f' values do not exhibit a nonlinear behavior, then one has to resort to subtraction methods developed in this paper described below. It should be borne in mind that subtraction methods usually lead to poor statistics, and hence the measured ASAXS data should have high statistical precision.

The decomposition of the ASAXS data into partial scattering functions requires subtraction of measured intensities at different X-ray energies by two methods: (1) subtraction after the normalization for the contrasts, $I_{s,1}$, and (2) subtraction with no normalization for the contrasts, $I_{s,2}$. It will be seen that the former ($I_{s,1}$) will lead to the scattering function associated with the form factor of the polymer phase (F_b^2) while $I_{s,2}$ with the nanoparticle phase (F_g^2).

Case I. Subtraction can be done using the SAXS data measured at an energy E_1 that is far away from the edge and at an energy E_2 near the edge in order have the maximum contrast

$$I_{s,1} \equiv \frac{I(Q,E_1)}{\rho_g^{\,2}(E_1)} - \frac{I(Q,E_2)}{\rho_g^{\,2}(E_2)}$$

$$= S_b(Q)\left[\left(\frac{\rho_b^{\,2}(E_1)}{\rho_g^{\,2}(E_1)} - \frac{\rho_b^{\,2}(E_2)}{\rho_g^{\,2}(E_2)}\right)F_b^{\,2} + 2\left(\frac{\rho_b(E_1)}{\rho_g(E_1)} - \frac{\rho_b(E_2)}{\rho_g(E_2)}\right)F_bF_g\right] \quad (7)$$

$$I_{s,2} \equiv I(Q,E_1) - I(Q,E_2)$$

$$= S_b(Q)[(\rho_g^{\,2}(E_1) - \rho_g^{\,2}(E_2))F_g^{\,2} + 2(\rho_b(E_1)\rho_g(E_1) - \rho_b(E_2)\rho_g(E_2))F_bF_g + (\rho_b^{\,2}(E_1) - \rho_b^{\,2}(E_2))F_g^{\,2}] \quad (8)$$

Equations 7 and 8 show that with a single subtraction method the extraction of F_g^2 and F_b^2 is still not possible due to the convolution of the structure factor of the polymer phase and the cross-terms involving the scattering amplitudes of the polymer and particles. However, it is possible to extract F_b^2 using a double-subtraction method by using SAXS data measured at an intermediate energy E_i that satisfies the condition $\rho_g^{-1}(E_1) - \rho_g^{-1}(E_i) = \rho_g^{-1}(E_i) - \rho_g^{-1}(E_2)$, or $\rho_g(E_i)$ is the harmonic mean of $\rho_g(E_1)$ and $\rho_g(E_2)$ [$\rho_g(E_i) = 2\rho_g(E_1)\rho_g(E_2)/(\rho_g(E_1) + \rho_g(E_2))$]. A double-subtraction leads to

$$I_{ds,1} \equiv \left[\frac{I(Q,E_1)}{\rho_g^{\,2}(E_1)} - \frac{I(Q,E_i)}{\rho_g^{\,2}(E_i)}\right] - \left[\frac{I(Q,E_i)}{\rho_g^{\,2}(E_i)} - \frac{I(Q,E_2)}{\rho_g^{\,2}(E_2)}\right]$$

$$= \rho_\alpha S_b(Q)F_b^{\,2} \quad (9)$$

where $\rho_\alpha \equiv \rho_b^{\,2}(E_1)\rho_g^{\,-2}(E_1) + \rho_b^{\,2}(E_2)\rho_g^{\,-2}(E_2) - \rho_g^{\,2}(E_i)\rho_g^{\,-2}(E_i)$. Extraction of F_g^2 is possible when $v_{Au} \ll 1$ and thus $\rho_b \sim \rho_{b,0}$. In this work, $v_{Au} < 0.01$. Likewise, delineation of F_g^2 requires measured data at three energies such that $\rho_g(E_1) - \rho_g(E_i) = \rho_g(E_i) - \rho_g(E_2)$, or $\rho_g(E_i)$ is the arithmetic mean of $\rho_g(E_1)$ and $\rho_g(E_2)$ [$\rho_g(E_i) = (\rho_g(E_1) + \rho_g(E_2))/2$]. A double subtraction of the data with no normalization for the contrast leads to

$$I_{ds,2} \equiv [I(Q,E_1) - I(Q,E_i)] - [I(Q,E_i) - I(Q,E_2)]$$

$$= S_b(Q)\rho_s(\rho_g(E_1) - \rho_g(E_2))F_g^{\,2} \quad (10)$$

where $\rho_s \equiv \rho_g(E_1) - \rho_g(E_i) = \rho_g(E_i) - \rho_g(E_2)$. Equation 10 shows that the intensity resulting from the double subtraction corresponds to the form factor of the nanoparticle phase [$F_g^2(Q)$] convoluted by the structure factor of the polymer matrix [$S_b(Q)$], but the cross-term involving the scattering amplitudes of the matrix and the nanoparticles in eq 8 gets removed. Elimination of form factor is critical as in any scattering experiment the convolution of form factors of multiple scattering species especially with similar size will make it difficult to characterize the system. Since $S_b(Q)$ will have peaks corresponding to the polymer morphology and oscillates about 1 at higher Q, it can be identified and separated to yield the scattering signal for the nanoparticle phase.

Case II. In contrast to case I, the single subtraction method for the macrophase separated system (Figure 1d) yields both F_g^2 and F_b^2 as follows:

$$I_{s,1} = \frac{(\rho_g^{\,2}(E_2) - \rho_g^{\,2}(E_1))\rho_{b,0}^{\,2}}{\rho_g^{\,2}(E_1)\rho_g^{\,2}(E_2)} S_b(Q)F_b^{\,2} \quad (11)$$

$$I_{s,2} = (\rho_g^{\,2}(E_1) - \rho_g^{\,2}(E_2))F_g^{\,2} \quad (12)$$

A double-subtraction method under the same conditions used for case I for the three energies leads to

$$I_{ds,1} = \rho_\alpha S(Q)F_b^{\,2} \quad (13)$$

$$I_{ds,2} = 2^{-1}(\rho_g(E_2) - \rho_g(E_1))^2F_g^{\,2} \quad (14)$$

Equations 9 and 13 show that $I_{ds,1} \sim S_b(Q)F_b^2$ in both cases I and II (either correlated or uncorrelated). When the distribution of the particles is uncorrelated with the structure of the block copolymer (case II), $I_{ds,1}(Q) \sim I_{s,1}(Q)$ and $I_{ds,2}(Q) \sim I_{s,2}(Q)$. Of course, for a completely phase-separated system in Figure 1d a double subtraction for case II is only an academic exercise as it is usually not necessary as the single-subtraction method already yields the scattering functions for the two distinct phases. However, if the intensities from the single- and double-subtraction methods are different, as observed in the case of

27.0% Au nanocomposite discussed later, it gives clues to the complexity in the system in its organization.

Experimental Section

Sample Preparation. For the synthesis of Au nanoparticles and PS−PVP/Au composites we follow the procedure developed by Yee[24] and Chiu et al.,[15] respectively. Briefly, Au nanoparticles were synthesized by the reduction of hydrogen tetrachloroaureate(III) trihydrate (Aldrich Chemical Co., Inc.) using 1.0 M lithium triethylborohydride in THF (Aldrich Chemical Co., Inc.). To stabilize nanoparticles, PSSH (M_n = 1500 g/mol, PDI = 1.10, Polymer Source, Inc.) is used as a protecting agent. Particles were purified by using methanol (≥99.8%, Aldrich Chemical Co., Inc.) to remove the residual ions and unbound thiol groups. SANS of the purified PSSH tethered Au nanoparticles in THF yielded a diameter of ~3.6 nm.[25] To prepare PS−PVP/Au composites, Au nanoparticles were redispersed in a THF solution containing PS−PVP [M_n (total molecular weight) = 71 000, f_{PS} (volume fraction of PS in PS−PVP) = 0.68, PDI (polydispersity index) = 1.07, Polymer Source, Inc.]. The enthalpic interactions between the PS grafts and the block copolymer allow them to sequester in the PS domain. We prepared PS−PVP/Au composites with two concentrations of the PSSH−Au particles ϕ_{Au} = 8.8% and 27.0% ($\phi_{Au} = V_{Au}/(V_{PS-PVP} + V_{Au})$, where V_{PS-PVP} and V_{Au} are the volumes of PS−PVP and PSSH−Au nanoparticles, respectively), representing two distinctly different particle distribution. Corresponding average volume fractions of pure Au in PS−PVP from TGA are 0.15% and 0.46% for the two samples. Composites with a film thickness of ~20 μm were cast on mica and epoxy substrates for the ASAXS and TEM measurements, respectively. Samples were then annealed at 150 °C for 3 days.

ASAXS. A quantitative ASAXS analysis requires information on the atomic scattering factor of Au that can either be measured or rigorously calculated. We measured its value using an EXAFS standard Au foil composed of Au particulates. Scattering data were measured for the Au foil and the PS−PVP/Au nanocomposites with ϕ_{Au} = 8.8% and 27.0% in a transmission geometry at 12-ID SAXS beamline[27] at the Advanced Photon Source at Argonne National Laboratory. For the Au foil, ASAXS was performed with 0.1 s exposure time in the range of 11.8−12 keV in 1 eV steps. For the nanocomposites, the ASAXS data were measured for 10 s per exposure at 14 different X-ray energies near the Au L_3 edge, 11.919 keV. Routine procedure was followed to reduce the scattering data by taking into account of the incident flux, absorption, dark current of the monitors, and the position-sensitive CCD area detector and sample thickness. Although it is desirable to have the ASAXS data placed on an absolute scale, the methodologies presented here can be used on data with no absolute calibration.

SAXS data on Au foil composed of Au particulates exhibits a power law scattering behavior in the low Q region (Figure 2). Since the scattering contrast for particle scattering is $f_{1,Au}^2(E)$, the scattering intensity at a given energy below, but in the vicinity of the edge, can be described to be proportional to the intensity at a reference energy E_L, as follows:[26]

$$I(Q,E) = mI(Q,E_L) + F(E) \tag{15}$$

where $m = \rho_g^2(E)/\rho_g^2(E_L)$; here ρ_g (electron densities of Au particle with respect to its surrounding matrix PS) is the contrast ratio and F the the fluorescence signal that is Q-independent in the range of this experiment. Since the matrix of the Au particulates in the EXAFS foil is air, the m value of the foil is $f_{1,Au}^2(E)/f_{1,Au}^2(E_L)$.

TEM. TEM images on the morphology of composites were obtained using a JEOL 2000 FX II microscope operated at 200 kV. Thin film samples cast on epoxy were cross-sectioned, followed by selective staining of the PVP domains using iodine vapor prior to the measurements.

Results and Discussion

Atomic Scattering Factor. Figure 2 shows representative

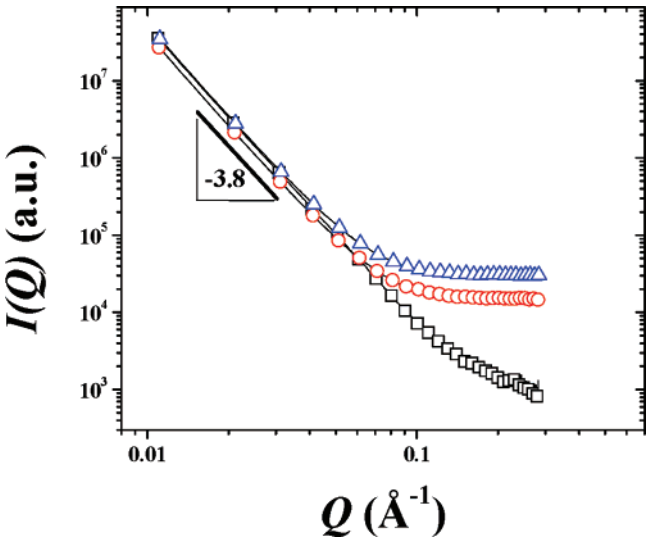

Figure 2. Representative SAXS data of an EXAFS standard Au foil composed of Au particulates measured at incident X-ray energies of 11.8 (square), 11.919 (circle), and 12.0 keV (triangle). The data exhibit a $Q^{-3.8}$ power law, and the intensity at a given Q in the low Q region monotonically decreases with increasing energy toward the L_3 edge of Au due to the decrease in the number of electrons contributing the scattering contrast. On the other hand, the scattering intensity at the high Q region increases with increasing X-ray energy due to monotonic increase in the fluorescence background.

SAXS patterns of the Au foil at three energies near the L_3 edge of Au. The measured data exhibit a $Q^{-3.8}$ power law scattering in the low Q region. As expected, the scattering intensity at a given Q in the low Q region monotonically decreases with increasing energy, and the lowest intensity occurs at an incident X-ray energy close to the edge. On the other hand, the flat background signal, dominated by the fluorescence, at the high Q region has the lowest intensity up until the edge energy and shoots up and remains high at and above the edge. It should be noted that while the SAXS intensity is proportional to the number density and square of the volume of particles, the fluorescence signal is proportional to the number density of the anomalous scatterers in the system.

The contrast ratio m and the fluorescence F as a function of energy for the Au foil were obtained by fitting eq 15 using the measured scattering intensities at Q = 0.02 Å^{-1} at over 200 incident X-ray energies [$I(Q,E)$] and that at the reference energy E_L = 11.8 keV [$I(Q,E_L)$]. The values for m derived from the fit are shown in Figure 3a. By using the energy-dependent theoretical scattering factor for Au from the McMaster table, we also calculated the contrast factor $m = f_{1,Au}^2(E)/f_{1,Au}^2(E_L)$ and the theoretical curve is also shown. The excellent agreement between the measured and calculated m values at the absorption edge indicates that the energy resolution of the monochromator is adequate for this study. In Figure 3b, we show the fitted F values and the fluorescent background along with the absorption spectra. It is clear that the measured fluorescence background data resemble the absorption spectra. Minor deviations between them at energies above the edge presumably are caused by the self-absorption.

While the ASAXS contrast for the Au particulates in the EXAFS foil will be constant at all Q values, regardless of their size, for the PS−PVP/Au composites it will be different and strongly depend on the sizes of the polymer phase and the Au nanoparticles. For instance, if Au particles are much smaller than the structure of block copolymer and are homogeneously mixed in the PS domain, one can neglect F_g in eq 3, and therefore the contrast would be the difference between $\rho_{e,PVP}$

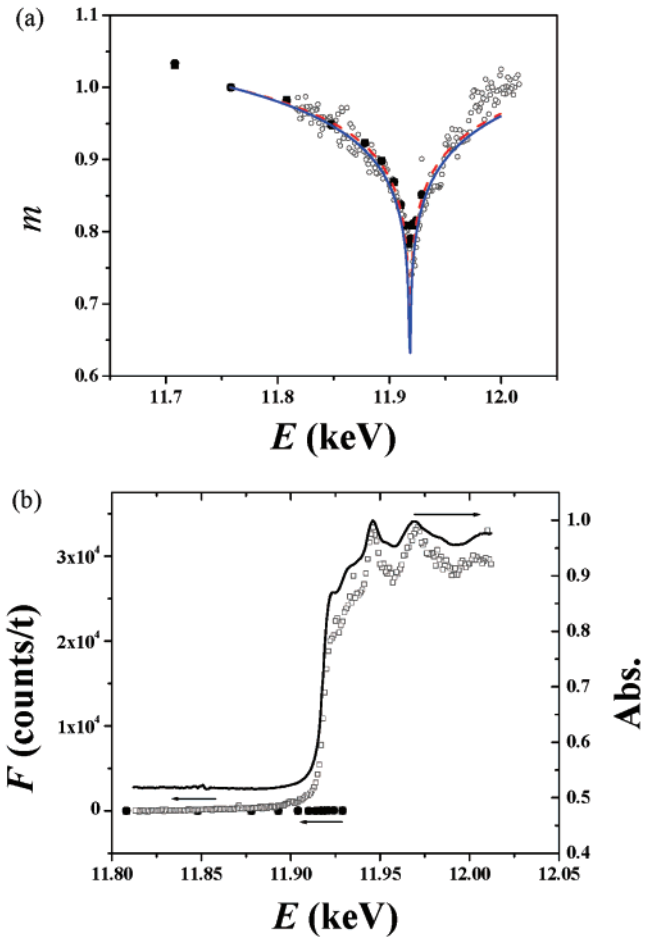

Figure 3. (a) Contrast ratio m values as a function of incident X-ray energy for the EXAFS standard Au foil (open square) obtained by using the measured scattering intensities at $Q = 0.02$ Å^{-1} at ~200 incident X-ray energies [$I(Q,E)$] and a reference energy $E_L = 11.8$ keV [$I(Q,E_L)$] to fit eq 15. By using the data from the McMaster table, we also calculated the contrast factor $m = f_{1,Au}^2(E)/f_{1,Au}^2(E_L)$, and the theoretical curve is shown as a solid line. Fitted m values for the PS−PVP composites with 8.8% and 27.0% Au loading (filled squares and circles) from the measured SAXS data at $Q \sim 0.07$ Å^{-1} using 14 incident energies and a reference energy $E_L = 11.758$ keV. The dotted lines are calculated $m = (\rho_g(E)/\rho_g(E_L))^2$ values for the composites assuming $\rho_g(E) = \rho_{e,Au} - \rho_{e,PS}$. (b) Fitted F values (filled squares and circles) of composites and an EXAFS foil (open square). Solid line is the absorption of the Au foil as a function of incident X-ray energy.

and $\bar{\rho}_{e,PS/Au}$ in the Q range of this experiment. Since the length scales of the polymer and the nanoparticles are different as in the present case (domain spacing of block copolymer is ~50 nm and the radius of Au particle is ~1.0 nm), scattering signals from those features appear at different Q ranges. The scattering intensity from the PS−PVP is dominant at $Q < 0.02$ Å^{-1} while that from the Au nanoparticles at $Q > 0.05$ Å^{-1}. Thus, the ASAXS contrast for the Au species at the high Q region is $\rho_g(E) = \rho_{e,Au} - \rho_{e,PS}$, whereas that at the low Q region would be $\rho_b(E) = \rho_{e,PVP} - \bar{\rho}_{e,PS/Au}$, provided that the Au particles are quite small and homogeneously mixed within the PS domain.

We fitted eq 15 using the SAXS data of two composites measured at 14 energies and that at the reference energy $E_L = 11.758$ keV at $Q \sim 0.07$ Å^{-1}, where nanoparticle scattering signal is dominant, and plotted m and F values in parts a and b of Figure 3, respectively. We also present the calculated m values for the composites assuming $\rho_g(E) = \rho_{e,Au} - \rho_{e,PS}$ in Figure 3a. It can be seen from Figure 3a that the fitted m values are independent of the concentration of Au nanoparticles.

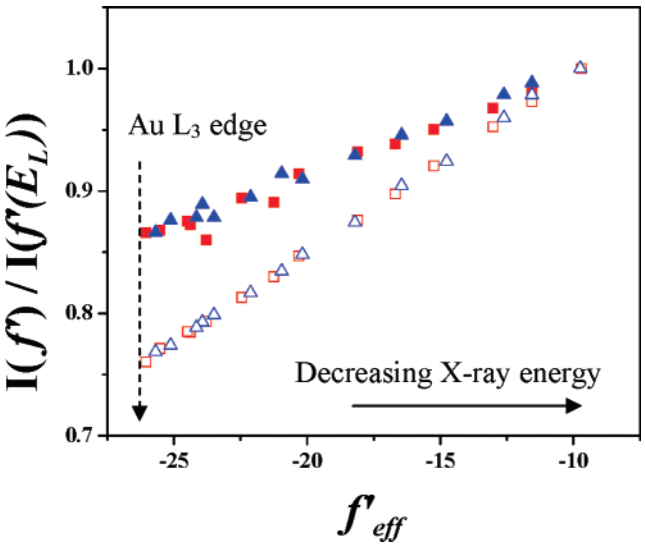

Figure 4. Ratio of intensities at a given Q for different incident X-ray energies with respect to a reference energy E_L as a function of the effective scattering factor f_{eff}: We chose intensities at $Q = Q^*$ (0.0132 Å^{-1}) (closed) for the PS−PVP phase and at $Q = 0.073$ Å^{-1} (open) for composites with 8.8% (square) and 27.0% (triangle) Au loading.

We determine the $f_{1,Au}$ values by using the fitted m values of the composites in Figure 3a and the theoretical $f_{1,Au}$ value of 66.537 from the McMaster tables[23,28] at the reference energy 11.758 keV. This experimentally derived $f_{1,Au}(E)$ values come out as smeared by the energy resolution of the beamline monochromator,[20] and we hereafter will refer to them as $f_{eff}(E)$. The effective dispersion term f'_{eff} can be calculated using the $f_{eff}(E)$ and f_0 values of Au.

ASAXS Analysis. Figure 4 presents the ratio of intensities at specific Q values for different incident X-ray energies with respect to the intensity at the reference energy, E_L (11.758 keV) vs f'_{eff}. Intensities at two representative Q positions are shown: $Q = Q^* = 0.0132$ Å^{-1} [$Q^* = 2\pi/d^*$, where d^* is d-spacing of PS−PVP] and $Q = 0.073$ Å^{-1}, where the scattering from PS−PVP and Au particles are dominant, respectively. The ratio is the lowest near the edge where the anomalous dispersion factor f'_{eff} is high, and it increases with decreasing incident X-ray energy where the effect of f'_{eff} will monotonically decrease (see Figure 4). Contrary to expectation based on eqs 4 and 6, the curves in Figure 4 exhibit only a linear behavior. The significant slope exhibited by the data at $Q = Q^*$ in Figure 4 where the polymer scattering is dominant suggests that Au particles do make significant contribution to the scattering intensity corresponding to the polymer phase. Thus, the Au particles, by virtue of their distribution in the PS microdomain, are correlated with the morphology of PS−PVP [see eqs 3 and 5, wherein the scattering intensity consists of a term involving a product of F_g and $S_b(Q)$ in eq 3 but not in eq 5]. However, the slopes corresponding to Q^* are smaller than that at $Q = 0.073$ Å^{-1} where the signal from Au is dominant. This is because the scattering contrasts for the Au-containing polymer phase $\rho_b(E) = \rho_{b,0} - \upsilon_{Au}\rho_g$ (when Au is homogeneously mixed with PS) and the Au particles $\rho_g(E) = \rho_{e,Au} - \rho_{e,PS}$ are quite different. It can be seen in Figure 4 that the slopes in the m values vs f'_{eff} data corresponding to $Q = 0.073$ Å^{-1} are identical for both composites. However, the slopes corresponding to $Q = Q^*$ for the Au-containing polymer phase are similar, but smaller. Similar slopes are unexpected for the two composites as at this Q the contrasts for the Au containing polymer phases should be different due to the difference in the Au composition in the two composites. The lack of composition dependence could be due to a combination

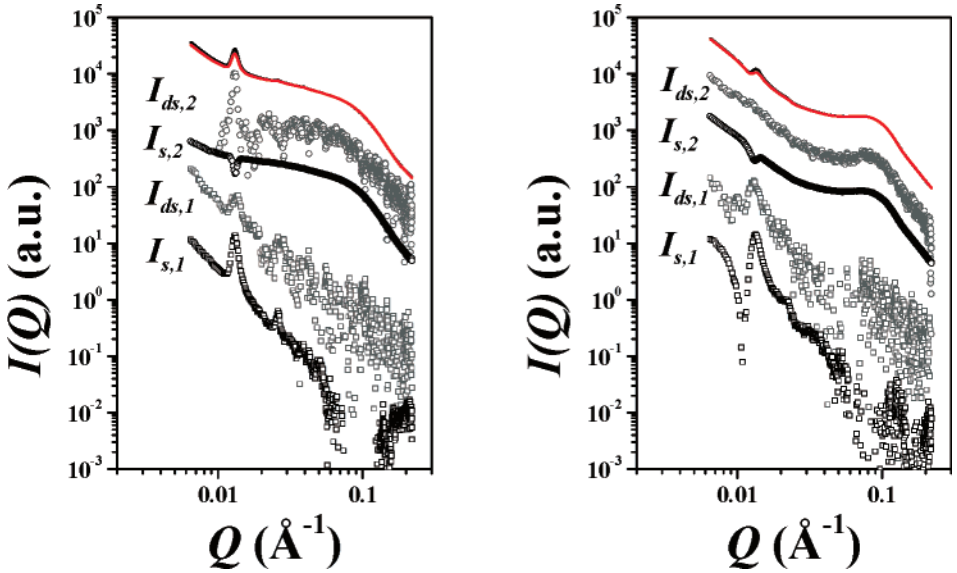

Figure 5. Scattering intensities normalized by the *m* values (lines) at $E = 11.919$ (red) and 11.758 keV (black) and single and double subtracted intensities (open squares) for the (a) 8.8% and (b) 27.0% Au composites.

of factors such as finite size of Au aggregates[29] whose scattering signal extends and continues to be dominant at $Q = Q^*$, disorder in the polymer morphology, and nonhomogeneous distribution of Au nanoparticles in the PS domains.

Because of the absence of nonlinearity in the curves in Figure 4 that prevents the use of fitting with a polynomial function, we resorted to the subtraction methods discussed above and the derived four subtracted intensities from eqs 7−10 for the 8.8% Au composite are shown in Figure 5a and those from eqs 11−14 for the 27.0% Au composite in Figure 5b. Subtracted intensities $I_{s,1}$and, $I_{s,2}$ were obtained from two patterns measured at $E = 11.758$ (E_1) and 11.917 keV (E_2), and double subtracted intensities $I_{ds,1}$and, $I_{ds,2}$ were obtained from three patterns with two at the above two energies and an intermediate one at 11.893 keV (E_i). The measured f'_{eff} values of Au nanoparticles at the above three energies in ascending order are 66.54, 62.93, and 58.95 (corresponding ρ_g values are 3.59, 3.37, and 3.14 Å^{-3}, respectively), and these values satisfy the condition for both the double-subtraction intensities $I_{ds,1}$ and $I_{ds,2}$ within ∼5% error. As expected, $I_{s,1}$and, $I_{s,2}$ in Figure 5a,b have better statistics than $I_{ds,1}$ and $I_{ds,2}$. While the former set enables identification of the morphology of the polymer, the latter set provides separated partial scattering functions of the phases. The dips in $I_{s,2}$ around $Q = Q^*$ for both samples suggest that the scattering signals of the Au particle and the block copolymer are correlated. In addition, $I_{s,1}$ helps to identify the higher order peaks (see Figure 5a) and hence the morphology of the block copolymer. Since $I_{ds,1}(Q)$ and $I_{ds,2}(Q)$ are not proportional to $I_{s,1}(Q)$ and $I_{s,2}(Q)$, respectively, for composites with 8.8% (Figure 5a) and 27.0% (Figure 5b) Au loadings, it can be concluded that both composites contain correlated domains. The structure factor of block copolymer, $S_b(Q)$, of the 8.8% sample is clearly visible in $I_{ds,2}$ (Figure 5a), which again evidences the presence of highly correlated structures. Although it is less visible in the $I_{ds,2}$ curve for the 27.0% Au composite, the presence of a dip in the $I_{s,2}(Q)$ curve in Figure 5b is a clear indication of the effect of $S_b(Q)$ convolution. It is likely that the presence of the power-law scattering from the aggregates at the same Q region as $S_b(Q)$ makes the peak less visible. On the basis of these observations, we surmise that the 27.0% Au composite resembles the model in Figure 1e consisting of both correlated (case I) and uncorrelated (case II) features.

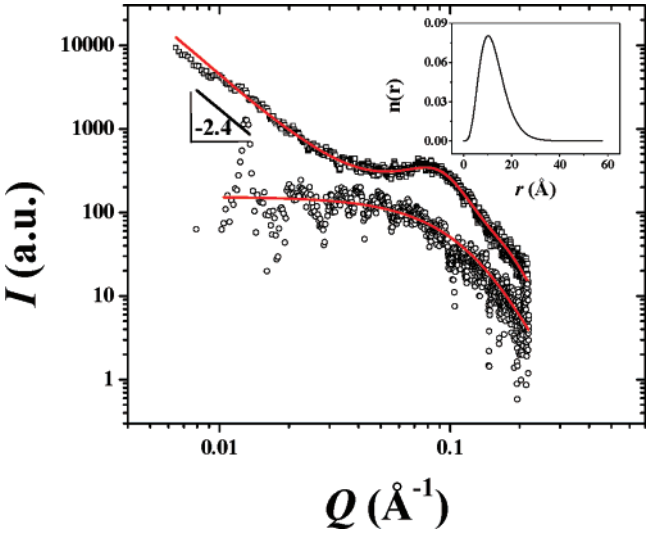

Figure 6. Partial scattering functions of Au nanoparticle in 8.8% (open circle) and 27.0% (open square) Au composites. Solid lines are fits using a form factor for polydisperse spheres and a hard sphere structure factor. Inset shows the particle size distribution of the pure Au particles (without accounting for the tethered polymers) with a mean diameter of 1 nm. The 27.0% Au composite has mass fractal aggregates as evidenced by $Q^{-2.4}$ a power law scattering in the low Q region.

Organization of Nanoparticles. The double subtracted intensities $I_{ds,2}$ corresponding to the partial scattering functions of the Au nanoparticle phases in 8.8% Au (Figure 5a) and 27.0% Au (Figure 5b) are plotted in Figure 6. While 8.8% Au composite does not show any power law scattering, the 27.0% Au composite exhibits a power law exponent α of −2.4, which suggests the existence of aggregates of Au nanoparticles.[30,31] According to fractal theory of aggregation,[31] the exponents of −1.75 and −2.08 correspond to a diffusion-limited and reaction-limited aggregation without rearrangement, respectively, and an exponent of −2.4 to a reaction-limited cluster−cluster aggregation with rearrangement. In the aggregated domains, because of the enthalpy of mixing, the PSSH tethered Au nanoparticles are segregated into domains and the smaller exponent is likely due to the large volume occupied by the PS species of the close-packed Au nanoparticles. The broad peak at $Q \sim 0.08$ Å^{-1} in the SAXS data of the 27.0% Au composite provides evidence for the interparticle correlation between the nanoparticles in the

segregated domains, but such a correlation peak does not exist for the 8.8% Au composite wherein the particles are well dispersed in the PS domain.

The nature of dispersion of Au nanoparticles was determined by fitting the $I_{ds,2}$ data for both samples in Figure 6 by using a combination of a power law and the polydisperse spherical particles with a hard-sphere structure factor. Here, $F_g^2(Q) = |F_{1,g}(Q)\sum_i^N e^{-iQd_i}|^2 \sim c_1/Q^\alpha + c_2P_g(Q)S_g(Q)$ has been assumed, where c_1 and c_2 are relative contributions to scattering from the aggregates and dispersed particles, respectively, $P_g(Q)$ is the form factor of Au nanoparticles with a Schultz distribution of sizes, $S_g(Q)$ is the structure factor of Au particles, and α is the power law exponent that describes the organization of the particles in the aggregates. The inset to Figure 6 shows the size distribution of Au particles as derived from the fits to the $I_{ds,2}$ data of the composites. Since this data corresponds solely to the Au moiety, the average radius of 1.0 nm is quite reasonable. Analysis of the $I_{ds,2}$ data for the 27.0% Au composite by including the Percus−Yevick hard-sphere structure factor[32] yields an average distance of 6.3 nm between the Au particles and a particle volume fraction of 11.8% in the PS domain. The average interparticle distance is consistent with a PS shell of Au nanoparticles with an average thickness of 2.1 nm. However, the SAXS-derived volume fraction of 11.8% for the Au moiety is quite large, given that the macroscopic value of the volume fraction of Au in the whole sample is about 0.46% from TGA. We attribute this large discrepancy to the following: SAXS is sensitive to the size, shape, concentration, and composition of the inhomogeneities in the samples. The larger the size of the inhomogeneity and its scattering contrast with respect to the surrounding matrix, the more dominant the scattering signal will be. In principle, if the Au particles are dispersed homogeneously throughout the polymer matrix as in micelles or proteins in solution, then the volume fraction from the SAXS will be similar to that from TGA. However, if the particles aggregate and form large and highly inhomogeneous domains in the sample, then the SAXS signal is sensitive to correlations in those domains rather than the whole sample. On the basis of this reasoning, we conjecture that the Au particles in 27.0% composite are highly aggregated, and their dispersion in the polymer phase is highly inhomogeneous and presumably confined within a small volume of the PS matrix as discussed below.

Morphology of the Block Copolymer Phase. The peak positions in the $I_{s,1}$ data for the two composites in Figure 5a,b allow the determination of the morphology of the polymer phase. The polymer phase for the 8.8% Au composite (Figure 5a) is lamellar while in the 27.0% Au composite (Figure 5b) it transforms to a hexagonally packed cylinder (HEX), based on the peak[33] at $\sqrt{3}Q^*$ (see Q^* and $\sqrt{3}Q^*$ peaks in the ASAXS data measured at 11.758 and 11.919 keV shown using solid arrows in Figure 7a). The incorporation of PSSH-coated Au particles in the PS domain causes its swelling, leading to the change in the interfacial curvature and hence the morphology. The diffraction peaks for the HEX morphology of the 27.0% Au composite are much broader and weaker than those for the 8.8% Au composite. The *d*-spacing of the 27.0% composite is 52.2 ± 2 nm, which is larger than the 48.3 nm for the 8.8% Au composite. Careful examination of SAXS data measured at E = 11.919 and 11.758 keV identifies two dips that are shown using broken arrows in Figure 7a. When compared to the data at 11.758 keV, the first dip seems to shift slightly to the smaller Q side in the data for 11.919 keV that is close to the L_3 edge of Au. We reason that these dips are associated with the form factor of a core−shell cylinder of the block copolymer, based on the following. In general, the first minimum of the form factor for a cylinder is not expected to occur at a Q smaller than the first-order diffraction peak because the diameter of a cylinder cannot be smaller than the *d*-spacing. When the Au

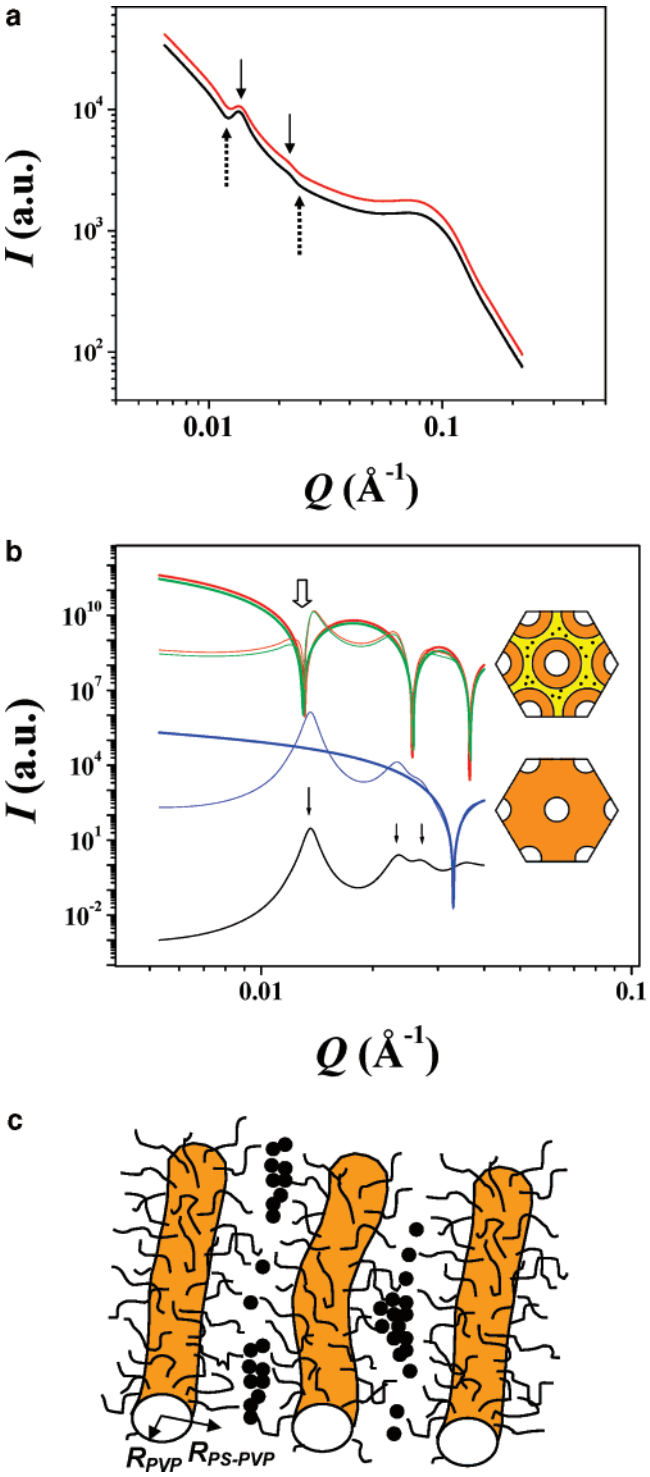

Figure 7. (a) SAXS data for the 27.0% Au composite (data shown as a solid line in Figure 5b) measured at E = 11.919 (red) and 11.758 keV (black). Solid and broken arrows indicate the positions of the diffraction peaks and the minima of the form factor corresponding to the morphology of the Au-containing polymer phase, respectively. (b) Simulations of $S_b(q)$ (black), $|F_b(q)|^2$ (thick lines), and $S_b(q)|F_b(q)|^2$ (thin lines) for the two models in the inset. To calculate $S_b(q)$, we used a *d*-spacing (d) of 53.25 nm and $\Delta d/d$ = 0.08. $|F_b(q)|^2$and $S_b(q)|F_b(q)|^2$ are calculated for two energies of 11.919 (red) and 11.758 keV (green) for the model at the top. (c) Schematic of the proposed model for the 27.0% Au composite depicting the morphology of the polymer phase and the nature of distribution of the Au particles.

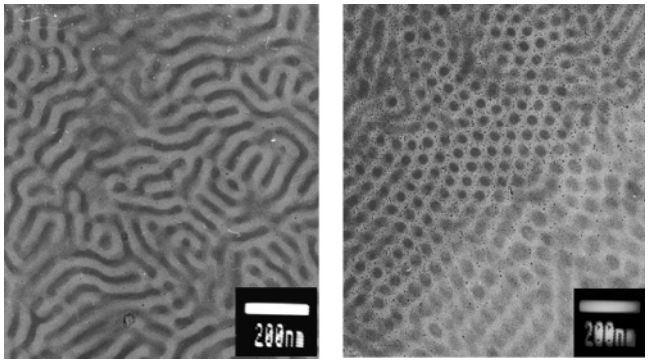

Figure 8. TEM images of PS−PVP composites with (a) 8.8% and (b) 27.0% Au nanoparticles exhibiting lamellar and HEX polymer phases, respectively.

particles are dispersed well in the PS domain as in the model at the bottom in Figure 7b, the positions of the minima should be the same as those for the neat block copolymer (blue curves in Figure 7b). On the other hand, if the form factor corresponds to a core−shell cylinder, then the Q position of the first minimum will be significantly smaller in the SAXS data (Q position for the first minimum for the cylinder is $\sim$0.032 Å^{-1} (model at the bottom, blue curve) while for a core−shell cylinder it is $\sim$0.011 Å^{-1}, as shown in Figure 7b for the model at the top, red curve). From the positions of minima and the known volume fractions of PVP and PS we determine an average radius of 11.6 nm for the PVP cylinder and a thickness of 16.4 nm for the PS brush. To illustrate the location of the nanoparticles, we divide the PS domain into a shell surrounding the PVP cylinder and a matrix region as in Figure 7b (model at the top). To resolve the location of the Au nanoparticles either in the shell or the matrix region of the PS domain, we calculated SAXS curves for a core−shell cylinder using the average electron densities of 0.43 and 0.41 Å^{-3} for two incident X-ray energies, 11.758 and 11.919 keV, respectively. As seen from the calculation, when the Au particles are located in the matrix, the first minimum will shift to the smaller Q side as the average electron density decreases (green and red curves in Figure 7b). On the other hand, when the particles exist in the PS brush region, the first mimimum will shift to the larger Q side (data not shown). On the basis of the agreement between the simulations and the behavior of the SAXS data in Figure 7a discussed earlier, we conclude that the Au particles are mostly confined at the middle of the PS matrix. Furthermore, as seen in the TEM images in Figure 8 for the composites, the core−shell cylinders are tortuous in the 27.0% composite as depicted in Figure 7c, and the aggregates of Au nanoparticles might be located at the high-curvature regions.

Conclusions

We investigated the nature of distribution of Au nanoparticles in a PS−PVP diblock copolymer using ASAXS. To analyze the ASAXS data, we developed theoretical and experimental methodologies to measure the scattering contrast of Au in a SAXS geometry and derive the partial scattering functions for the Au nanoparticles and PS−PVP phase. We considered two representative composites with different Au concentrations. In the 8.8% Au composite, the particles disperse well at the middle region of the lamellar PS domain. However, in the 27.0% Au composite, the morphology of PS−PVP transforms to HEX, which we identified by using the form factor of a core−shell cylinder composed of a PVP core and a PS brush and diffraction peaks. The nanoparticles seem to aggregate at the bent regions of the tortuous cylinder shaped PS−PVP phase while the aggregated Au nanoparticles are located at the inter-cylinder domains constituted by the PS.

Acknowledgment. This work benefited from the use of IPNS, APS, and CMT funded by DOE-BES under Contract DE-AC02-06CH11357.

References and Notes

(1) Ciebien, J. F.; Clay, R. T.; Sohn, B. H.; Cohen, R. E. *New J. Chem.* **1998**, 685−691.
(2) Torquato, S.; Hyun, S.; Donev, A. *Phys. Rev. Lett.* **2002**, *89*, 266601-1−266601-4.
(3) Sohn, B. H.; Cohen, R. E. *Chem. Mater.* **1997**, *9*, 264−269.
(4) Buxton, G. A.; Balazs, A. C. *Phys. Rev. E* **2003**, *67*, 031802-1−031802-12.
(5) Thompson, R. B.; Ginzburg, V. V.; Matsen, M. W.; Balazs, A. C. *Science* **2001**, *292*, 2469−2472.
(6) Thompson, R. B.; Ginzburg, V. V.; Matsen, M. W.; Balazs, A. C. *Macromolecules* **2002**, *35*, 1060−1071.
(7) Lee, J. Y.; Thompson, R. B.; Jasnow, D.; Balazs, A. C. *Macromolecules* **2002**, *35*, 4855−4858.
(8) Schultz, A. J.; Hall, C. K.; Genzer, J. *Macromolecules* **2005**, *38*, 3007−3016.
(9) Chan, Y. N. C.; Schrock, R. R.; Cohen, R. E. *Chem. Mater.* **1992**, *4*, 24−27.
(10) Tsutsumi, K.; Funaki, Y.; Hirokawa, Y.; Hashimoto, T. *Langmuir* **1999**, *15*, 5200−5203.
(11) Sohn, B. H.; Seo, B. H. *Chem. Mater.* **2001**, *13*, 1752−1757.
(12) Bockstaller, M. R.; Lapetnikov, Y.; Margel, S.; Thomas, E. L. *J. Am. Chem. Soc.* **2003**, *125*, 5276−5277.
(13) Sohn, B.-H.; Choi, J.-M.; Yoo, S. I.; Yun, S.-H.; Zin, W.-C.; Jung, J. C.; Kanehara, M.; Hirata, T.; Teranishi, T. *J. Am. Chem. Soc.* **2003**, *125*, 6368−6369.
(14) Lin, Y.; Boker, A.; He, J.; Sill, K.; Xiang, H.; Abetz, C.; Li, X.; Wang, J.; Emrick, T.; Long, S.; Wang, Q.; Balazs, A.; Russell, T. P. *Nature (London)* **2005**, *434*, 55−59.
(15) Chiu, J. J.; Kim, B. J.; Kramer, E. J.; Pine, D. J. *J. Am. Chem. Soc.* **2005**, *127*, 5036−5037.
(16) Dingenouts, N.; Ballauff, M. *Acta Polym.* **1993**, *44*, 178−183.
(17) Hendrickson, W. A. *Science* **1991**, *254*, 51−58.
(18) Hendrickson, W. A.; Horton, J. R.; Lemaster, D. M. *EMBO. J.* **1990**, *9*, 1665−1672.
(19) Haubold, H.-G.; Wang, X. H. *Nucl. Instrum. Methods Phys. Res. B* **1995**, *97*, 5−54.
(20) Dingenouts, N.; Patel, M.; Rosenfeldt, S.; Pontoni, D.; Narayanan, T.; Ballauff, M. *Macromolecules* **2004**, *37*, 8152−8159.
(21) Brumberger, H.; Hagrman, D.; Goodisman, J.; Finkelstein, K. D. *J. Appl. Crystallogr.* **2005**, *38*, 147−151.
(22) http://skuld.bmsc.washington.edu/scatter/AS_periodic.html.
(23) Cromer, D. T.; Liberman, D. *J. Chem. Phys.* **1970**, *53*, 1891−1898.
(24) Yee, C. K.; Jordan, R.; Ulman, A.; White, H.; King, A.; Rafailovich, M.; Sokolov, J. *Langmuir* **1999**, *15*, 3486−3491.
(25) Lo, C.-T.; Lee, B.; Dietz, N. L.; Seifert, S.; Winans, R. E.; Thiyagarajan, P. Manuscript under review.
(26) Lee, B.; Seifert, S.; Riley, S. J.; Tikhonov, G.; Tomczyk, N. A.; Vajda, S.; Winans, R. E. *J. Chem. Phys.* **2005**, *123*.
(27) Seifert, S.; Winans, R. E.; Tiede, D. M.; Thiyagarajan, P. *J. Appl. Crystallogr.* **2000**, *33*, 782−784.
(28) Jemian, P. R. http://www.uni.aps.anl.gov/cgi-bin/fprime.
(29) Pontoni, D.; Narayanan, T.; Petit, J.-M.; Grubel, G.; Beysens, D. *Phys. Rev. Lett.* **2003**, *90*, 1883011−1883014.
(30) Schaefer, D. W.; Martin, J. E.; Wiltzius, P.; Cannell, D. S. *Phys. Rev. Lett.* **1984**, *52*, 2371−2374.
(31) Wijnen, P.; Beelen, T. P. M.; Rummens, K. P. J.; Saeijs, H.; Vansanten, R. A. *J. Appl. Crystallogr.* **1991**, *24*, 759−764.
(32) Kinning, D. J.; Thomas, E. L. *Macromolecules* **1984**, *17*, 1712−1718.
(33) Hashimoto, T.; Kawamura, T.; Harada, M.; Tanaka, H. *Macromolecules* **1994**, *27*, 3063−3072.

MA062916H